# Nitride Synthesis Under High-Pressure High-Temperature Conditions – Unprecedented *in-situ* Insight into the Reaction

*Sebastian J. Ambach,[1] Reinhard M. Pritzl,[1] Shrikant Bhat,[2] Robert Farla,[2] Wolfgang Schnick[1]**

1: Department of Chemistry, University of Munich (LMU), Butenandtstraße 5-13, 81377 Munich, Germany

2: Deutsches Elektronen Synchrotron (DESY), Notkestraße 85, 22607, Hamburg, Germany

KEYWORDS

Nitrides, Nitridophosphates, High-Pressure, High-Temperature, In-situ, Reaction Mechanism

ABSTRACT

High-pressure high-temperature (HP/HT) syntheses are essential for modern high-performance materials. Phosphorus nitride, nitridophosphate and more generally nitride syntheses benefit greatly from HP/HT conditions. In this contribution, we present the first systematic *in-situ* investigation of a nitridophosphate HP/HT synthesis, using the reaction of zinc nitride $Zn_3N_2$ and phosphorus(V)nitride $P_3N_5$ to the nitride semiconductor $Zn_2PN_3$ as a case study. At a pressure of 8 GPa and temperatures up to 1300 °C the reaction was monitored by energy-dispersive powder X-ray diffraction (ED-PXRD) in a large-volume press at beamline P61B at DESY. The experiments investigate the general behavior of the starting materials under extreme conditions and give insight into the reaction. During cold-compression and subsequent heating the starting materials remain crystalline above their ambient-pressure decomposition point, until a sufficient minimum temperature is reached and the reaction starts. The reaction proceeds via ion diffusion at grain boundaries with an exponential decay of the reaction rate. Raising the temperature above the minimum required value quickly completes the reaction and initiates single crystal growth. After cooling and decompression, which did not influence the resulting product, the recovered sample was analyzed by EDX-spectroscopy.

INTRODUCTION

Several high-performance ceramics such as nano-polycrystalline diamond, cubic boron nitride, $BC_2N$, and refractory spinel-type γ-$Si_3N_4$ require synthesis at high pressures.[1–6] The scale-up for production under gigapascal pressure is much more time consuming and expensive than for ceramics manufactured at ambient pressures, which are issues that can be alleviated through understanding of formation mechanisms. Unlike ambient pressure synthesis of ceramics,

however, the formation of solid-state compounds under high-pressure was never monitored *in-situ* and therefore reaction mechanisms are proposed based on *ex-situ* information. The installation of large-volume-presses (LVP) at synchrotron facilities, such as beamline station P61B at PETRA III, DESY, enable *in-situ* monitoring of high-pressure high-temperature reactions.[7]

Over the past decades several models for solid-state kinetics and reaction mechanisms at ambient pressure have been developed, either from theoretical calculations or experimental data.[8] This encompasses simple order-based models, derived from kinetics in liquid homogeneous systems. Nucleation models are most commonly used to explain crystallization, phase transitions, decompositions, adsorptions, hydrations and desolvations.[9–18] In these models, all processes start at one or more nucleation sites, which provide minima for reaction activation energies due to crystal imperfections or surfaces. Special cases are grouped under the term contraction models, which assume a nucleation start at the surface of a crystal with the reaction proceeding to its center.[8] The most common model for the formation of new compounds during syntheses is the diffusion model.[19,20] A fundamental work of Tamman suggests the melt free diffusion of ions at grain boundaries of different reactants into each other, forming a layer of the product.[21] As this layer grows, the reaction rate drastically decreases due to lengthened diffusion pathways. Additionally, a reactant-depended minimum temperature is needed to initially start the diffusion and the subsequent diffusion rate exhibits a strong temperature dependence. To describe the thickness of the product layer and thus the reaction speed, the empirical equation

$$z = a \cdot \ln(t) + c \qquad (1)$$

($z$: layer thickness; $a$: temperature-dependent constant; $t$: reaction time; $c$: constant) was published. Based on further experimental data in subsequent work, Jander proposed a slightly modified equation, describing the layer thickness as quadratic dependent on the reaction time:

$$z^2 = 2 \cdot t \cdot c \qquad (2)$$

($z$: layer thickness; $t$: reaction time; $c$: constant depending on diffusion coefficients).[22] This model was used for various solid-state reaction mechanisms investigations later on.[23–25]

Like most of the ambient-pressure experiments above, the major part of high-pressure research is focused on oxidic materials.[26] However, another large class of compounds benefits from or sometimes even requires high pressures during syntheses: nitrides, and in particular the subclass of phosphorus nitrides and nitridophosphates.[27,28] The high temperatures needed for their synthesis are in direct contrast to their susceptibility for thermal decomposition, beyond which releasing molecular $N_2$ becomes thermodynamically favored because of its stable triple bond (942 kJ/mol).[29] Additionally, in phosphorus nitrides and nitridophosphates, $P^{+V}$ is prone to reduction to $P^{+III}$, elemental P or even $P^{-III}$ in phosphides, due to the reductive environment provided by the nitride anions (electron affinity of $N^{3-}$ +0.07 eV).[30] According to Le Chatelier's principle, the decomposition and formation of gaseous $N_2$ during syntheses can be countered by applying pressure. Thus, syntheses typically are carried out under high temperatures and high pressures up to the gigapascal (GPa) range.

Due to the isoelectronic elemental combination P/N and Si/O, the structural diversity of nitridophosphates is predicted to be at least as large as the one of oxosilicates, consequently suggesting a field of application, which is in no way inferior. As of today, this includes the application as gate insulator in metal-insulator semiconductor field-effect transistors (MISFETs), as an oxygen eliminating material during the production of incandescent and tungsten halogen

lamps and discussions regarding a use in pyrotechnics safety, as flame retardant, as gas storing material for ammonia, as candidate for a warm-white phosphor in solid state lighting and lithium ion conductivity.[31–39]

Over the past thirty years, several synthetic methods for phosphorus nitrides and nitridophosphates under high-pressure high-temperature conditions have emerged, including some mechanistic suggestions: the solid-state metathesis, the $Li_3N$ self-flux method, the nitride route, the azide route as well as $NH_4Cl$, HCl and $NH_4F$ assisted syntheses.[40–45] Starting from $LiPN_2$ and a metal halide, the solid-state metathesis uses the formation of the corresponding lithium halide as reaction driving force.[42] Additionally, the lithium halide, which is molten at reaction conditions, acts as flux agent supporting single crystal growth. Similarly, small amounts of $NH_4Cl$ have been proven to be suitable as mineralizer by facilitating the reversible formation and cleavage of P/N bonds.[45] A comparable assumption is made for the $Li_3N$ self-flux method, which employs $Li_3N$ both as starting material and flux agent.[39] Additionally it was suggested, that the $Li_3N$ flux can preserve P/N building blocks from the starting materials.[38] Transferring the well-known ion exchange to high-pressure high-temperature syntheses, it was shown that a preservation of a P/N framework is possible.[46] Recently, *in-situ* generated HCl and HF was used to activate inert starting materials such as BN or even TiN.[43,44] It is assumed that reactive intermediate species are formed during the reaction process. The azide route uses $P_3N_5$ and a metal azide as reactant, which is suggested to decompose under elevated pressure, releasing molecular $N_2$, the partial pressure of which further inhibits the decomposition of nitrides.[35] Using this method, Wendl *et al.* proposed the to date single detailed reaction mechanism on the formation of nitridophosphates, derived from pressure-quenched samples.[47] $SrP_6N_8(NH)_4$ is assumed to be an intermediate species that condenses to $SrP_8N_{14}$ by replacing imide groups with

$PN_4$ tetrahedra in the crystal structure. To date, however, there is no experimental proof of any thesis.

In this contribution, we present the first systematic *in-situ* study of a high-pressure high-temperature nitridophosphate synthesis. The nitride route, reacting $P_3N_5$ and a metal nitride, seemed most suitable for *in-situ* XRD observation, as no molten state or decomposition are supposed to be involved. In two experiments, the synthesis of $Zn_2PN_3$, a nitride semiconductor, is monitored as model system *in-situ* to investigate the general behavior of the starting materials, the formation of products and the impact of cooling and decompression under extreme conditions and gain insight into the condensation mechanism.[40,48] The recovered samples are subsequently analyzed by EDX spectroscopy and SEM images.

## EXPERIMENTAL SECTION

**Preparation of phosphorus(V) nitride $P_3N_5$.** The binary phosphorus(V) nitride $P_3N_5$ was prepared as partially crystalline powder according to Stock *et al*. by ammonolysis of phosphorus pentasulfide ($P_4S_{10}$, Acros Organics, >98%) in a constant flow of ammonia gas ($NH_3$, Air Liquide, 99.999%).[49] To exclude oxygen and moisture, a boat of silica glass, placed in a silica tube, was dried at 1000 °C for 8 h under a reduced pressure of $10^{-3}$ mbar. Afterwards, the silica boat was filled with 8 g of $P_4S_{10}$ and centered inside the outer tube within a resistance furnace. The apparatus was saturated with $NH_3$ by a constant flow for 1 h at ambient temperature and consequently heated with 7 °C/min to 850 °C. After a reaction time of 4 h, the furnace was cooled down with 7 °C/min. The orange powdery product was analyzed for contaminations from elements other than P and N by powder X-ray diffraction (PXRD) and elemental CHNS-analysis (measured: C: 0%, H: 0%, N: 43.16%, S: 0%; calculated: C: 0%, H: 0%, N: 42.98%, S: 0%).

**High-pressure high-temperature experiments.** The assembly with the starting materials for the synthesis of $Zn_2PN_3$ (eq. 1) was prepared as published by Sedlmaier *et al.*[40]

$$2\ Zn_3N_2 + P_3N_5 \rightarrow 3\ Zn_2PN_3 \qquad (3)$$

Stoichiometric amounts of $Zn_3N_2$ (Alfa Aesar, 99%) and partially crystalline α-$P_3N_5$ were ground together under argon atmosphere in a glovebox ($O_2/H_2O$ < 1 ppm). An h-BN crucible was half filled with the powder mixture and half filled with MgO, both separated by a small h-BN disc and finally closed with a lid of the same material. Small pieces of tantalum foil were attached to the top and bottom of the h-BN crucible to locate the sample by *in-situ* X-ray radiography. High-Z materials (such as Ta) exhibit greater X-ray absorption and thus appear dark in the image. The h-BN components were held in the center of a graphite heater by two MgO disks. For electrical contact, Mo rods within MgO disks were attached on the top and bottom of the graphite furnace. The described assembly was centered in a drilled-through octahedron (MgO, 5% $Cr_2O_3$ doped, 14 mm edge length), placed in the middle of eight electrically insulated Co-doped WC cubes with truncated corners (8% Co, 32 mm edge length, truncated edge length 8 mm). A detailed schematic sketch of the assembly can be found in the supporting information (Figure S1). The sample was compressed to the target pressure of 8 GPa by the Hall-type six-ram large-volume-press (LVP) Aster-15 (Voggenreiter, Mainleus, Germany), located at beamline P61B at DESY, using the 6-8 Kawai-type compression geometry.[7] The actual sample pressure was determined from the measured unit cell volume of an MgO pressure marker and its known equation of state.[50] The sample temperature was controlled by manually adjusting the heating power, using a calibration curve of heating power vs. temperature. In-situ observations were performed by energy-dispersive powder X-ray diffraction (ED-XRD) using two high-purity

germanium solid-state detectors (Ge-SSD, Mirion, Canberra). The assembly was visualized with a white-beam X-ray microscope (Optique Peter, Lentilly, France).

Two experiments were carried out: the first for screening the reaction timeframe, temperature region and involved phases, and the second, to *in-situ* monitor the formation of $Zn_2PN_3$ with a sampling frequency of 8-10 diffraction patterns per minute (i.e. 6 – 8 s acquisitions).

**Experiment for general overview.** A detector angle $2\theta$ of ~5.13°, an incident beam slit aperture of 50 x 300 $\mu m^2$, and an exposure time of 100 s were selected for all measurements in the first experiment. During compression, powder diffraction patterns were acquired at hydraulic oil pressures of 50, 100, and 200 bar in the master ram. After reaching the target MgO pressure, the sample was heated manually to the reaction temperature of 1200 °C in steps of 100 °C. After a 30-minute hold time, the temperature was increased to 1300 °C and the sample finally cooled down to ambient temperature in 200 °C decrements (Figure 1). During both heating and cooling, a diffraction pattern was collected after each temperature step, with an additional 10 consecutive patterns measured immediately after the reaction temperature (1200 °C) was reached. After cooling, the sample was decompressed and a final diffraction pattern was measured at ambient pressure.

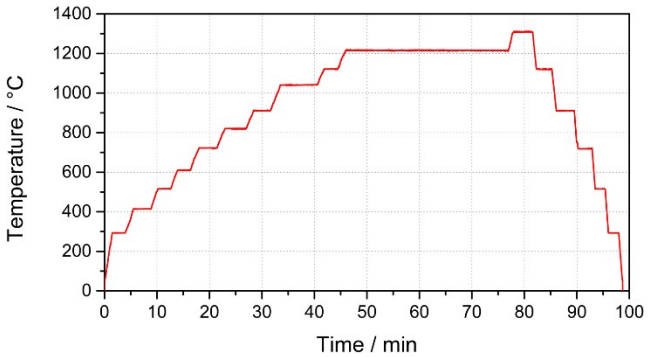

**Figure 1.** Overview of the temperature curve for the first experiment. Heating was performed manually by adjusting the heating power and converted to a specific temperature using a calibration curve previously established (Figure S2).

**Time-resolved experiment.** All measurements of the second experiment were performed with a detector angle $2\theta$ of ~3.00° and an incident beam slit aperture of 200 x 700 µm$^2$. Diffraction spectra were collected continuously throughout the heating period with a 2 s exposure time. Due to system limitations, this resulted in a pattern acquired every 7-10 s (including acquisition time), equating to a sampling frequency of 6-8 patterns/minute. After compression to the target pressure (8 GPa), the sample was manually heated as shown in Figure 2. After cooling and decompression, the sample analyzed by energy-dispersive X-ray spectroscopy (EDX).

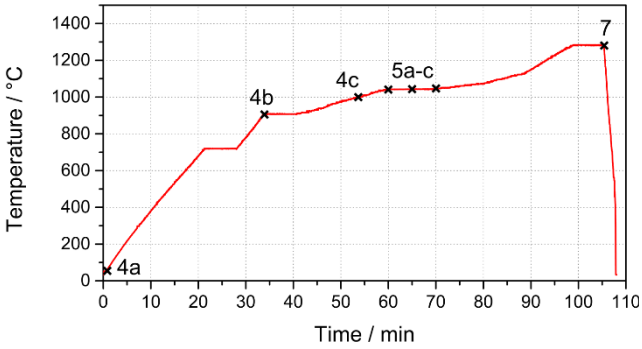


**Figure 2.** Temperature profile of the second experiment. Heating was performed manually by adjusting the heating power. Temperatures were evaluated using a calibration curve. Spectra of the highlighted points are discussed in the results section with the respective Figures.

**Energy-dispersive X-Ray spectroscopy (EDX) and scanning electron microscopy (SEM).** For EDX measurements, the sample was recovered from all assembly parts under argon atmosphere in a glovebox. The powdered sample was prepared on an electrically conductive, self-adhesive carbon foil on an aluminum sample holder and coated with a thin layer of carbon (electron beam evaporator, BAL-TEC MED 020, BalTex AG, Pfäffikon, Swiss). EDX-spectra

and SEM-images were recorded with a Dualbeam Helios Nanolab G3 UC electron microscope (FEI, USA) equipped with an X-Max 80 SDD detector (Oxford Instruments, UK). The data and image capturing were done using the Aztec software (Oxford instruments, UK).[51]

## RESULTS AND DISCUSSION

**Experiment for general overview.** Both starting materials are known for their thermal decomposition at ambient pressure ($Zn_3N_2$: 400 °C under $O_2$ atmosphere, 600 °C under $N_2$ atmosphere; $P_3N_5$: 800 °C).[28,52] As published by Sedlmaier *et al.*, a reaction temperature of 1200 °C, thus well above the decomposition points, is required to form $Zn_2PN_3$. Since any experimental insights into possible decompositions and other processes under high-pressure high-temperature conditions are lacking, our first experiment monitored the entire synthesis including compression and heating phase (Figures 3a-d). The most intense reflections of $Zn_3N_2$ are each marked with the corresponding lattice plane indices. No reflections of $P_3N_5$ can be observed, which may be due to pressure-induced phase amorphization combined with poor X-ray scattering factors of the light atoms P and N and the partially crystalline nature of the starting material. In addition, fluorescence peaks of lead caused by the experimental setup and small unassignable reflections (marked with an asterisk) are visible in each diffraction pattern.

Figure 3a shows the diffraction patterns of three different compression points with their respective pressures. Comparing them, two well-known pressure-related effects can be observed. First, a compression of the unit cell, which causes a shift of the reflections to higher energies, corresponding to smaller d spacings. Second, the introduction of microscopic crystal strain, grain crushing and a dislocation increase, which leads to broadened reflections with reduced intensity.

In this case, intensities decrease by about 30% from 1.3 GPa to 8.1 GPa. $Zn_3N_2$ shows no signs of a phase transition, (pre)reaction, or decomposition up to 8.1 GPa. Although no reflections of $P_3N_5$ can be observed, we assume that this is also the case here, since both show comparable materials properties.

Heating the assembly (Figure 3b) at a pressure of 8 GPa proves the stabilizing effect of pressure on $Zn_3N_2$. Until approaching the reaction temperature of 1200 °C, $Zn_3N_2$ shows no signs of interaction with other materials, phase transitions or intermediate formation in the diffraction patterns. The intensity ratios of $Zn_3N_2$ reflections begin to differ from those measured under ambient conditions, which may be explained by material texture. In addition, temperature-related effects on $Zn_3N_2$ reflections are observed, which partially reverse the pressure-related effects. Elevated temperatures usually lead to an expansion of the unit cells caused by increased thermal motion, and thus to a shift of reflections to lower energies. It also anneals dislocations, as evidenced by a decreased FWHM of the reflections and their increased intensity. Up to 1100 °C, the thermal effects have little impact on the position and shape of the reflections. A pressure-induced shift of +1.3 keV and intensity decrease of about 30% compared to a temperature-induced shift of –0.7 keV and an intensity increase of about 10% is visible in the 332 main reflection.

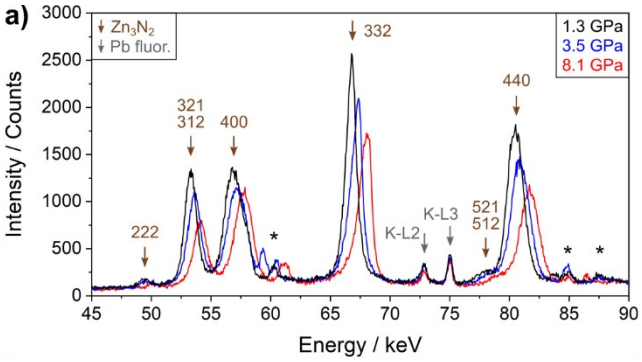
a)
Zn3N2
Pb fluor.
1.3 GPa
3.5 GPa
8.1 GPa
Intensity / Counts
Energy / keV
222
321
312
400
332
K-L2
K-L3
521
512
440
*

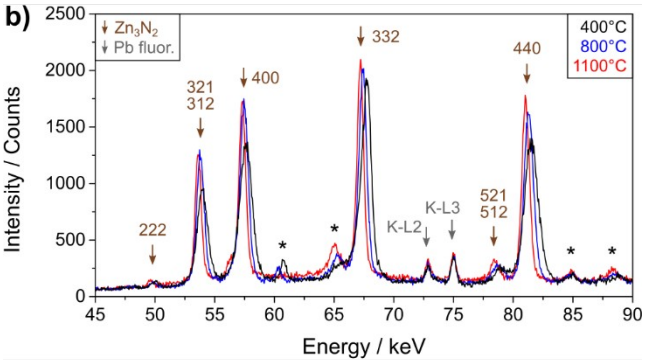
b)
Zn3N2
Pb fluor.
400°C
800°C
1100°C
Intensity / Counts
Energy / keV
222
321
312
400
332
K-L2
K-L3
521
512
440
*

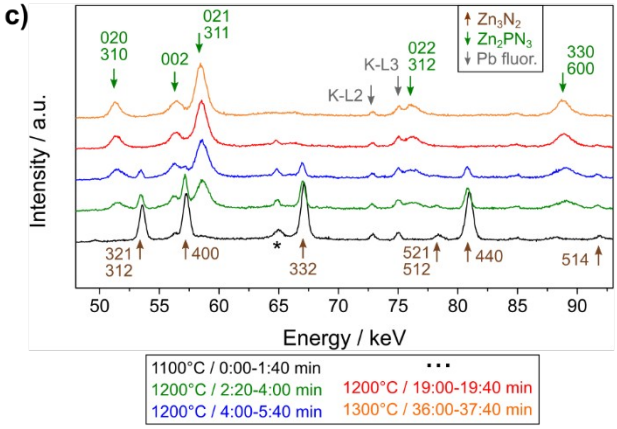
c)
Zn3N2
Zn2PN3
Pb fluor.
Intensity / a.u.
Energy / keV
020
310
002
021
311
K-L2
K-L3
022
312
330
600
321
312
400
*
332
521
512
440
514
1100°C / 0:00-1:40 min
1200°C / 2:20-4:00 min
1200°C / 4:00-5:40 min
...
1200°C / 19:00-19:40 min
1300°C / 36:00-37:40 min

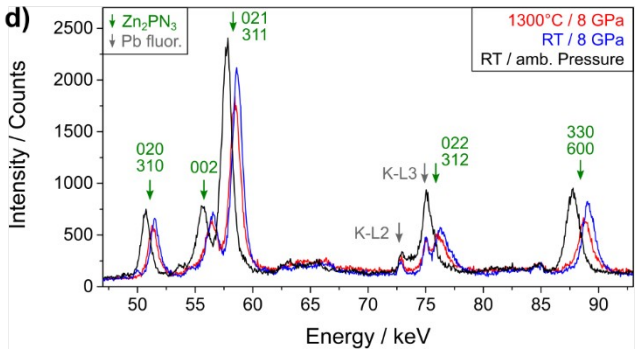
d)
Zn2PN3
Pb fluor.
1300°C / 8 GPa
RT / 8 GPa
RT / amb. Pressure
Intensity / Counts
Energy / keV
020
310
002
021
311
K-L2
K-L3
022
312
330
600

**Figure 3.** Energy-dispersive diffraction patterns ($2\theta$ ~5.13°) of the first experiment. Reflection indices of $Zn_3N_2$ (brown), $Zn_2PN_3$ (green), and Pb-fluorescence peaks (grey) are indicated with arrows. Reflections that cannot be assigned are marked with an asterisk. **a)** Assembly compression at 1.3 GPa (black), 3.5 GPa (blue) and 8.1 GPa (red). Pressures were determined using MgO as a pressure marker. **b)** Heating from ambient temperature to 1100 °C (400 °C black, 800 °C blue, 1100 °C red) at a pressure of 8 GPa. Temperatures were adjusted using a calibration curve of heating power vs. temperature **c)** Reaction of $Zn_3N_2$ and $P_3N_5$ to $Zn_2PN_3$ with time and temperature codes. **d)** Temperature- and pressure-quenching the assembly from 1300 °C/8 GPa (red) to ambient temperature/8 GPa (blue) to ambient pressure (black).

The reaction occurs within a short period of approximately 5 minutes (published reaction time: 10 minutes) when the assembly temperature reaches 1200 °C (Figure 3c).[40] During this period, the intensity of the $Zn_3N_2$ reflections continuously decreases until they completely disappear, while the $Zn_2PN_3$ reflections appear and gain intensity. According to the ED-XRD patterns, neither a time interval with completely amorphous materials nor any crystalline intermediate species are involved in this transition. Comparatively broad, low intensity reflections of newly formed $Zn_2PN_3$ increase in intensity and show a reduced FWHM as time progresses. This corresponds to small $Zn_2PN_3$ domains at the start, which grow with time. Increasing the temperature to 1300 °C or beyond does not have any visible effect on $Zn_2PN_3$ or initiate its decomposition. However, a detailed look at the processes involved in the transition from $Zn_3N_2$ and $P_3N_5$ to $Zn_2PN_3$, is not possible on a time scale of 100 s per measurement and will be further investigated in the second experiment.

Temperature-quenching and decompressing the assembly to ambient conditions has very little effect on the sample (Figure 3d). The single crystals do not seem to grow further, as neither an

overall intensity increase nor a decreased FWHM of the $Zn_2PN_3$ reflections is observed. The changed intensities of single reflections, especially 021/311 and 330/600, may be attributed to texture effects. After decompression, the 022/312 reflection overlaps with the K-L3 fluorescence line of Pb, which explains the striking intensity change. In addition, the temperature-induced shift to higher energies as well as the pressure-induced shift to lower energies are observed upon cooling and decompressing, respectively.

This overview experiment on the formation of $Zn_2PN_3$ has shown that until the reaction temperature is reached, $Zn_3N_2$ and possibly also $P_3N_5$ are only affected by pressure and temperature related effects and otherwise remain stable. The reaction occurs on a short time scale, while longer heating periods promote domain growth.

**Time-resolved experiment.** Since the processes involved in the formation of $Zn_2PN_3$ from $Zn_3N_2$ and $P_3N_5$ occur in the time frame of a few minutes, a second experiment was performed with a reduced exposure time of 2 s (resulting in a diffraction pattern every 7-10 s) and a modified heating program (Figure 3). To achieve sufficient intensity at such short exposure times, the incident beam slit aperture was increased from 50 x 300 $\mu m^2$ to 200 x 700 $\mu m^2$.

After compression to 8.4 GPa, the main reflections of $Zn_3N_2$ and partially crystalline $P_3N_5$ were identified (Figure 4a). In contrast to the overview experiment, this experiment was carried out with an enhanced detector system, allowing the observation of $P_3N_5$ reflections.[7] In addition, Pb fluorescence peaks from the experimental setup and MgO peaks originating from parts of the assembly are visible. Since MgO is not in contact with the starting materials at any time and is only visible due to the larger slit aperture, it does not affect the reaction, as evidenced by a constant MgO peak throughout the experimental period. The same applies to the BN and an

unknown peak (marked with an asterisk), which remain constant over the entire experimental period.

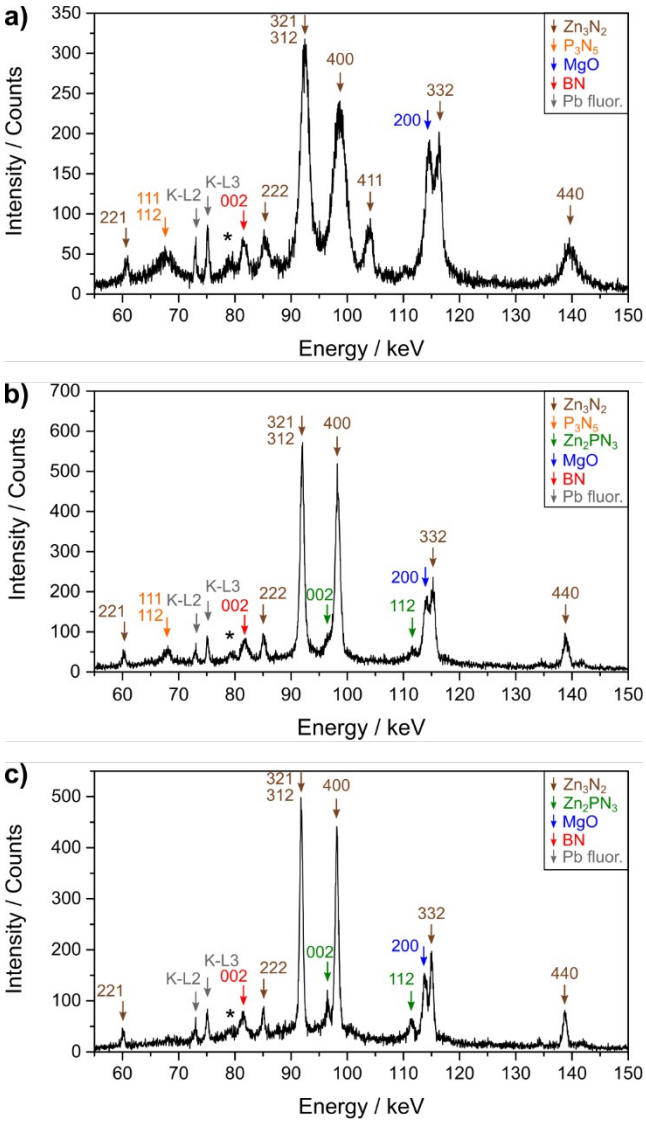


**Figure 4.** Energy-dispersive diffraction patterns ($2\theta$ ~3.00°) of the sample at 8.4 GPa before reaching the reaction temperature. The reflections of different materials are colour coded: $Zn_3N_2$ (brown), $P_3N_5$ (orange), MgO (blue), Pb fluorescence peaks (grey), unassigned reflections (asterisks). **a)** At ambient temperature, the starting materials $Zn_3N_2$ and $P_3N_5$ are identified. **b)** At 900 °C, the first reflections of the product $Zn_2PN_3$ appear. **c)** At 1000 °C reflections of $P_3N_5$ disappear, while the reflections of $Zn_2PN_3$ become more distinct.

Near the reaction temperature (900 °C), heating was temporarily interrupted to ensure that a uniform temperature was established throughout the sample (Figure 4b). As in the first experiment, recrystallization of the starting materials and a strong influence of texture can be observed. This can be seen especially in the fact that reflections 321, 312 and 400 double their intensity compared to ambient temperature and the 411 peak even disappears completely. In addition, the 002 and 112 peaks of the product $Zn_2PN_3$ are already visible, however with low intensity. Even after an extended time at a constant temperature of 900 °C, these reflections do not grow noticeably. As discussed later, this may be explained by the formation of a small product layer at grain boundaries by ion diffusion. Since 900 °C might be too low to sustain a significant diffusion rate through the thickening $Zn_2PN_3$ layer, the reaction rate drastically decreases to almost standstill.

The same is true for further heating of the assembly to 1000 °C (Figure 4c). The reflections of $Zn_2PN_3$ increase in intensity, as higher temperatures allow further diffusion until the $Zn_2PN_3$ layer reaches a certain thickness again, which leads to the almost standstill. Aside from the already advanced reaction, the range of 900-1000 °C marks a turning point in the behavior of the starting materials. While up to 900 °C reflections gain intensity due to recrystallisation, above 1000 °C a reverse effect is observed. The maximum intensity (321/312 reflection) drops by about 14% in this temperature range. The same applies for $P_3N_5$, whose main reflections disappear completely. This supports the observation of a started reaction at grain boundaries, consuming small fractions of the starting materials.

At a temperature of 1050 °C, the reaction initiates throughout the entire sample (Figure 5a). The measurements reveal a further decrease in the intensity of $Zn_3N_2$ reflections, while the existing $Zn_2PN_3$ reflections gain intensity and new ones emerge due to a higher proportion of

$Zn_2PN_3$ in the sample. After a reaction time of 5 minutes, a significant change in the diffraction pattern becomes evident, following the trend of intensity changes observed in previous measurements (Figure 5b). Another 5 minutes later, the reaction rate has substantially decreased, and the intensity changes of reflections are hardly noticeable anymore (figure 5c).

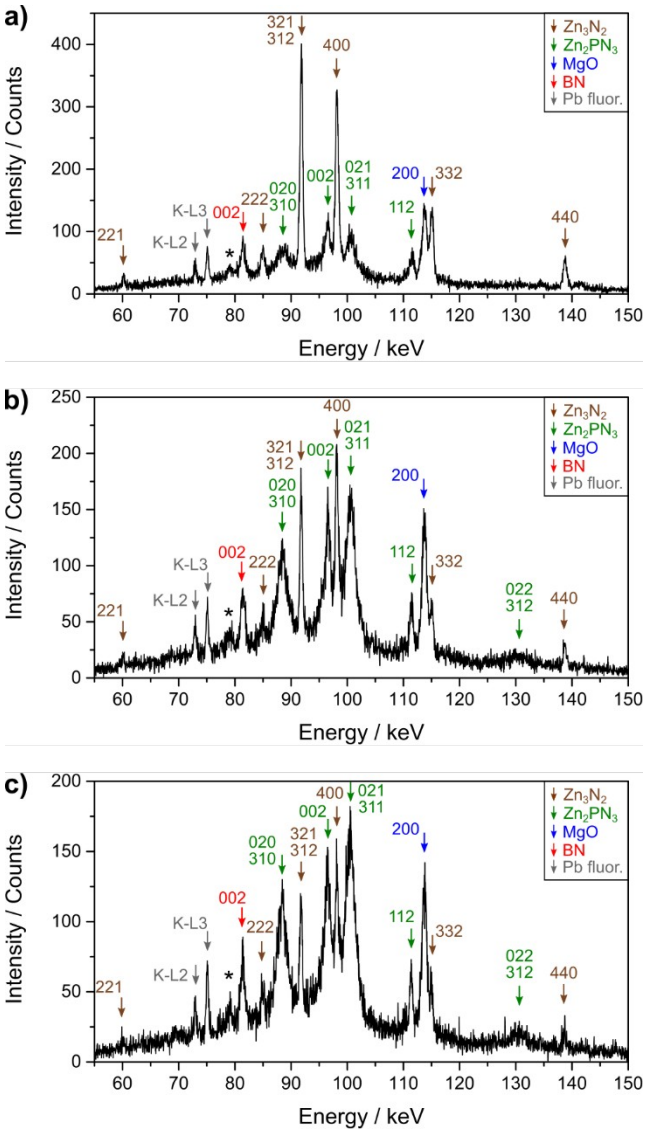


**Figure 5.** Energy-dispersive diffraction patterns ($2\theta$ ~3.00°) of the reaction period. The reflections of different materials are colour coded: $Zn_3N_2$ (brown), $P_3N_5$ (orange), MgO (blue), Pb fluorescence peaks (grey), unassigned reflections (asterisks). **a)** Reaction start at 1050 °C. **b)** Diffraction pattern after 5 min at 1050 °C. **c)** Diffraction pattern after 10 min at 1050 °C.

The observations can be interpreted and explained as a transition from $Zn_3N_2$ and $P_3N_5$ towards $Zn_2PN_3$ by ion diffusion, a reaction mechanism regularly observed for solid-state syntheses at ambient pressure, e.g. for $NiAl_2O_4$.[24] Once the required temperature is reached, ion diffusion initiates at grain boundaries between $Zn_3N_2$ and $P_3N_5$, leading to the formation of a $Zn_2PN_3$ layer. As this layer grows, the diffusion pathways become longer, resulting in a slowdown of the reaction. Although the mobile ion species involved in the present reaction could not be determined, we assume that $Zn^{2+}$ and $N^{3-}$ ions of the $Zn_3N_2$ are primarily responsible, as the electrostatic diffusion barrier for $P^{5+}$ ions might be too high and covalent bonds in $PN_4$ tetrahedra may not easily be broken. In the case of $NiAl_2O_4$ formation, the layer thickness shows a quadratic correlation with the reaction time. To perform a comparable analysis, the intensities of the 321/312 $Zn_3N_2$ and 020/310 $Zn_2PN_3$ peaks were monitored during the reaction to derive the amount of $Zn_3N_2$ remaining and the amount of $Zn_2PN_3$ already formed. In case of the present reaction, a quadratic fit is not sufficient to describe the observed intensity changes; instead, an exponential growth/decay function of the general form

$$y = y_0 + A \cdot \exp(t/B) \qquad (4)$$

was used (Figure 6) ($y$: degree of reaction α; $y_0$: degree of reaction α at $t = 0$; $A$,$B$: constants; $t$: time in minutes). The difference in reaction behavior may be attributed to the difference in bond nature of the elements involved. While the oxidic bonds of $NiAl_2O_4$ are of predominantly ionic nature, P−N bonds have a significant covalent character due to similar energies of the 3p(P) and 2p(N) orbitals.[53] The partially covalent $Zn_2PN_3$ layer exhibits a higher energy barrier than the ionic $NiAl_2O_4$ layer, thus the diffusion rate slows down much more with increasing product layer

thickness. Equation 4 closely recalls the Avrami model, which is typically used to describe isothermal phase transitions.[54]

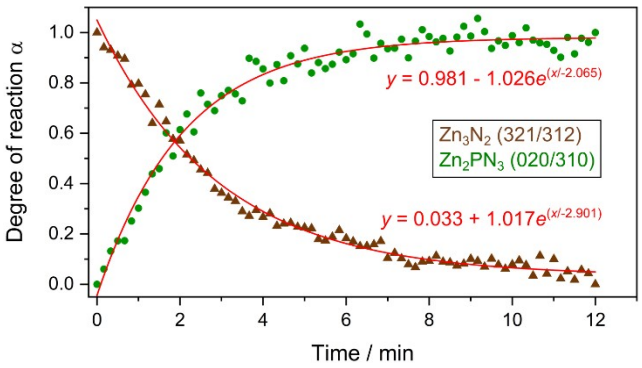


**Figure 6.** Exponential decrease in reaction rate. The areas of 321/312 $Zn_3N_2$ and 020/310 $Zn_2PN_3$ reflections were observed from the beginning of the reaction (reaching 1050 °C) to the end (increasing temperature above 1050 °C). The degree of reaction $\alpha$ was calculated by normalizing the areas. The data were fitted exponentially with $y = y_0 + A \cdot \exp(t/B)$.

The monitored time frame was set between reaction start, i.e. reaching 1050 °C (Figure 5a), and the start of a further temperature increase (Figure 5c), resulting in a total reaction time of 12 minutes. The 321/312 $Zn_3N_2$ reflection and 020/310 $Zn_2PN_3$ reflection were chosen for observation as both are main reflections of the respective materials and can be clearly separated from neighboring reflections. In the given time interval, the integrated area of the two peaks was calculated for each diffraction pattern. The results were normalized with respect to the initial and final points, respectively, defining the degree of reaction $\alpha$ between 0 and 1.

In accordance with the first experiment, the reaction proceeds rapidly within 5 minutes. Thereafter, the rate decreases drastically, leaving unreacted precursors inside the grains, which is visible in the diffraction patterns. The proposed reaction mechanism implies that no intermediate species are involved in the transition to $Zn_2PN_3$, which is supported by the absence of additional reflections in the ED-XRD patterns. In addition to the absence of intermediates, the background

of all patterns also remains constant at about 50 counts during the reaction, indicating that no significant amorphous parts are involved in the ion diffusion process.

Newly formed $Zn_2PN_3$ shows rather broad reflections with low intensity, indicating low crystallinity. Without an increase in temperature, the reaction could almost come to a standstill and the current state could be preserved for an extended period of time. This also implies an either endothermic or only slightly exothermic reaction, as a highly exothermic behavior would have the same effect as an increase in temperature. When the latter is done manually, the reaction proceeds rapidly towards $Zn_2PN_3$ and all reflections of $Zn_3N_2$ disappear, as higher temperatures allow for a higher diffusion rate and distance, enabling precursor grains to react completely. In addition, the reflections begin to show a much smaller FWHM, corresponding to single crystal growth of $Zn_2PN_3$ (Figure 7).

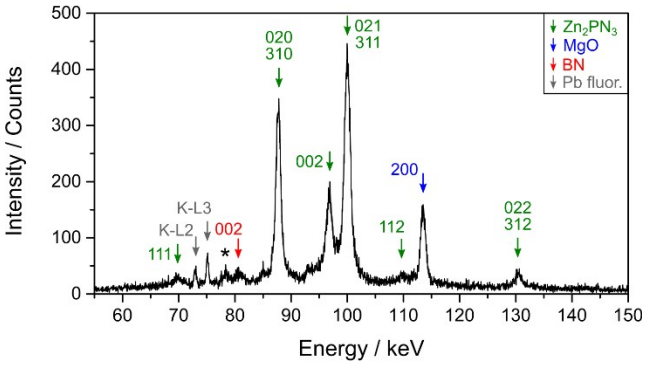


**Figure 7.** Diffraction pattern of the sample at 1300 °C. Reflections of $Zn_2PN_3$ (green), MgO (blue) and Pb-fluorescence peaks (gray) are marked with arrows. Two asterisks indicate not assignable reflections.

**Energy-dispersive X-Ray spectroscopy (EDX) and scanning electron microscopy (SEM).** To further investigate the single crystal formation of $Zn_2PN_3$, the sample was temperature quenched and decompressed, recovered from the assembly parts and examined by scanning electron

microscopy. Figure 8 shows agglomerated $Zn_2PN_3$ single crystals up to 30 µm in length. This is consistent with the observed single crystal growth at temperatures above 1200 °C.

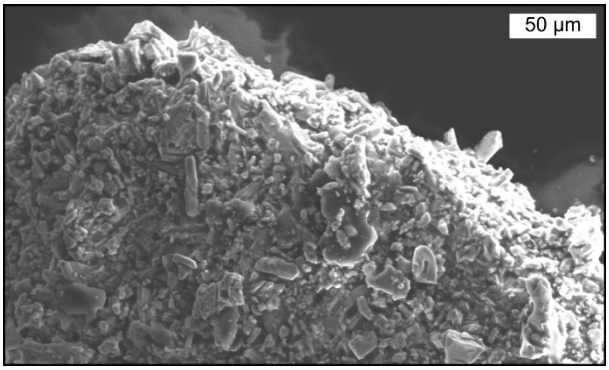


**Figure 8.** SEM image of the pressure- and temperature-quenched sample. Agglomerated single crystals of $Zn_2PN_3$ up to 30 µm length were formed during the reaction.

To prove that the crystallites shown in Figure 8 are $Zn_2PN_3$, EDX spectra were collected on different single crystals of the agglomerated particle, giving the sum formula $Zn_{2.0(2)}P_{0.8(2)}N_{1.1(3)}O_{0.2(6)}$. The anionic deviation from $Zn_2PN_3$ may be explained by two effects. In our experience, the light elements N and O are underestimated by the experimental setup compared to the heavier Zn. Secondly, $Zn_2PN_3$ is sensitive to air and an unavoidable short contact causes slow surface hydrolysis.

## CONCLUSION

Using the large-volume press at the DESY beamline P61B in combination with synchrotron radiation, the first in-situ insights into the high-pressure high-temperature nitridophosphate synthesis are provided.

The starting materials remain crystalline above their ambient pressure decomposition point until they start to react. At sufficient temperature, most of the starting materials react within a

short period of time. However, the reaction rate slows down exponentially at an intermediate constant temperature (1050 °C), which can be described by an exponential equation of the general form $y = y_0 + A \cdot \exp(t/B)$. Mechanistically, the reaction proceeds via ion diffusion at grain boundaries, which was often observed for solid-state syntheses at ambient pressure. Neither crystalline intermediate species nor a significant amorphous state is involved in the transition. Raising the temperature above the minimum required reaction temperature (1050 °C), the reaction is quickly completed. Raising the temperature even further does not have much influence on the resulting product, and the same applies to cooling and decompression. Further experiments to analyze the influence of mineralizers such as $NH_4Cl$ or the reaction within a salt melt (high-pressure metathesis, $Li_3N$ self-flux) may give an even deeper understanding of reaction processes and more possibilities to optimize reaction conditions.

## ASSOCIATED CONTENT

The supporting information includes a schematic figure of the assembly, the temperature calibration curves, the pressure program of the LVP, an *in-situ* X-ray image of the assembly and the EDX data of the pressure quenched sample.

AUTHOR INFORMATION

**Corresponding Author**

*E-mail: wolfgang.schnick@uni-muenchen.de

**ORCID**

Shrikant Bhat: 0000-0002-1229-9842

Robert Farla: 0000-0003-1245-2111

Wolfgang Schnick: 0000-0003-4571-8035

**Author Contributions**

The manuscript was written through contributions of all authors. All authors have given approval to the final version of the manuscript.

**Notes**

The authors declare no competing financial interest.

ACKNOWLEDGMENTS

We gratefully acknowledge the financial support by Deutsche Forschungsgemeinschaft (project SCHN 377/18-1). We acknowledge DESY (Hamburg, Germany), a member of the Helmholtz Association HGF, for the provision of experimental facilities. Parts of this research were carried out at beamline P61B (Proposal No. I-20210953) with the support from the Federal Ministry of

Education and Research, Germany (BMBF, grants no.: 05K16WC2 & 05K13WC2). Furthermore, we thank Christian Minke for the SEM and EDX measurements.

REFERENCES

1. Solozhenko, V. L.; Dub, S. N.; Novikov, N. V. Mechanical properties of cubic $BC_2N$, a new superhard phase. *Diam. Relat. Mater.* **2001**, *10*, 2228–2231.
2. Liu, G.; Kou, Z.; Yan, X.; Lei, L.; Peng, F.; Wang, Q.; Wang, K.; Wang, P.; Li, L.; Li, Y.; Li, W.; Wang, Y.; Bi, Y.; Leng, Y.; He, D. Submicron cubic boron nitride as hard as diamond. *Appl. Phys. Lett.* **2015**, *106*, 121901.
3. Dubrovinskaia, N.; Solozhenko, V. L.; Miyajima, N.; Dmitriev, V.; Kurakevych, O. O.; Dubrovinsky, L. Superhard nanocomposite of dense polymorphs of boron nitride: Noncarbon material has reached diamond hardness. *Appl. Phys. Lett.* **2007**, *90*, 101912.
4. Zerr, A.; Miehe, G.; Serghiou, G.; Schwarz, M.; Kroke, E.; Riedel, R.; Fueß, H.; Kroll, P.; Boehler, R. Synthesis of cubic silicon nitride. *Nature* **1999**, *400*, 340–342.
5. Zerr, A.; Kempf, M.; Schwarz, M.; Kroke, E.; Göken, M.; Riedel, R. Elastic Moduli and Hardness of Cubic Silicon Nitride. *J. Am. Ceram. Soc.* **2002**, *85*, 86–90.
6. H. Sumiya. Novel Development of High-Pressure Synthetic Diamonds “Ultra-hard Nano-polycrystalline Diamonds”. *SEI Tech. Rev.* **2012**, *74*, 15–23.
7. Farla, R.; Bhat, S.; Sonntag, S.; Chanyshev, A.; Ma, S.; Ishii, T.; Liu, Z.; Néri, A.; Nishiyama, N.; Faria, G. A.; Wroblewski, T.; Schulte-Schrepping, H.; Drube, W.; Seeck, O.; Katsura, T. Extreme conditions research using the large-volume press at the P61B endstation, PETRA III. *J. Synchrotron Radiat.* **2022**, *29*, 409–423.
8. Khawam, A.; Flanagan, D. R. Solid-state kinetic models: basics and mathematical fundamentals. *J. Phys. Chem. B* **2006**, *110*, 17315–17328.
9. Erukhimovitch, V.; Baram, J. Crystallization kinetics. *Phys. Rev. B* **1994**, *50*, 5854–5856.
10. Anderson, V. J.; Lekkerkerker, H. N. W. Insights into phase transition kinetics from colloid science. *Nature* **2002**, *416*, 811–815.
11. Burnham, A. K.; Weese, R. K.; Weeks, B. L. A Distributed Activation Energy Model of Thermodynamically Inhibited Nucleation and Growth Reactions and Its Application to the β−δ Phase Transition of HMX. *J. Phys. Chem. B* **2004**, *108*, 19432–19441.
12. Graetz, J.; Reilly, J. J. Decomposition kinetics of the $AlH_3$ polymorphs. *J. Phys. Chem. B* **2005**, *109*, 22181–22185.
13. Wang, S.; Gao, Q.; Wang, J. Thermodynamic analysis of decomposition of thiourea and thiourea oxides. *J. Phys. Chem. B* **2005**, *109*, 17281–17289.

14. Cantor, B. Heterogeneous nucleation and adsorption. *Philos. Trans. R. Soc. Lond. A* **2003**, *361*, 409–417.

15. Wu, C.; Wang, P.; Yao, X.; Liu, C.; Chen, D.; Lu, G. Q.; Cheng, H. Effects of SWNT and metallic catalyst on hydrogen absorption/desorption performance of $MgH_2$. *J. Phys. Chem. B* **2005**, *109*, 22217–22221.

16. Peterson, V. K.; Neumann, D. A.; Livingston, R. A. Hydration of tricalcium and dicalcium silicate mixtures studied using quasielastic neutron scattering. *J. Phys. Chem. B* **2005**, *109*, 14449–14453.

17. Sögütoglu, L.-C.; Steiger, M.; Houben, J.; Biemans, D.; Fischer, H. R.; Donkers, P.; Huinink, H.; Adan, O. C. G. Understanding the Hydration Process of Salts: The Impact of a Nucleation Barrier. *Cryst. Growth Des.* **2019**, *19*, 2279–2288.

18. Sullivan, R. A.; Davey, R. J.; Sadiq, G.; Dent, G.; Back, K. R.; Horst, J. H. ter; Toroz, D.; Hammond, R. B. Revealing the Roles of Desolvation and Molecular Self-Assembly in Crystal Nucleation from Solution: Benzoic and p -Aminobenzoic Acids. *Cryst. Growth Des.* **2014**, *14*, 2689–2696.

19. Hardel, K. Mechanisms of Reactions in the Solid State. *Angew. Chem. Int. Ed. Engl.* **1972,** *11*, 173–179; *Angew. Chem.* **1972**, *84*, 227–233.

20. Schäfer, H. Preparative Solid State Chemistry: The Present Position. *Angew. Chem. Int. Ed. Engl.* **1971,** *10*, 43–50; *Angew. Chem.* **1971**, *83*, 35–42.

21. Tammann, G.; Westerhold, F.; Garre, B.; Kordes, E.; Kalsing, H. Chemische Reaktionen in pulverförmigen Gemengen zweier Kristallarten. *Z. Anorg. Allg. Chem.* **1925**, *149*, 21–98.

22. Jander, W. Reaktionen im festen Zustande bei höheren Temperaturen. Reaktionsgeschwindigkeiten endotherm verlaufender Umsetzungen. *Z. Anorg. Allg. Chem.* **1927**, *163*, 1–30.

23. Garre, B. Vorgänge im festen Zustande. *Z. Anorg. Allg. Chem.* **1927**, *163*, 43–48.

24. Petit, F. S.; Randklev, E. H.; Felten, E. J. Formation of $NiAl_2O_4$ by Solid State Reaction. *J. Am. Ceram. Soc.* **1966**, *49*, 199–203.

25. Koch, E.; Wagner, C. Über die Bildung von $Ag_2HgJ_4$ ans AgJ und $HgJ_2$ durch Reaktion im festen Zustand. *Z. Phys. Chem.* **1936**, *34*, 317–321.

26. Hemley, R. J. Ultrahigh Pressure Mineralogy: Physics and Chemistry of the Earth's Deep Interior, 37th Ed., *The Mineralogical Socienty of America* Washington, DC, **1998**.

27. Horvath-Bordon, E.; Riedel, R.; Zerr, A.; McMillan, P. F.; Auffermann, G.; Prots, Y.; Bronger, W.; Kniep, R.; Kroll, P. High-pressure chemistry of nitride-based materials. *Chem. Soc. Rev.* **2006**, *35*, 987–1014.

28. Kloß, S. D.; Schnick, W. Nitridophosphates: A Success Story of Nitride Synthesis. *Angew. Chem. Int. Ed.* **2019**, *58*, 7933–7944; *Angew. Chem.* **2019**, *131*, 8015–8027.

29. Kildahl, N. K. Bond Energy Data Summarized. *J. Chem. Educ.* **1995**, *72*, 423.

30. Bratsch, S. G. Standard Electrode Potentials and Temperature Coefficients in Water at 298.15 K. *J. Phys. Chem. Ref. Data* **1989**, *18*, 1–21.

31. Kobayashi, T.; Hirota, Y. Inversion-mode InP MISFET employing phosphorus-nitride gate insulator. *Electron. Lett.* **1982**, *18*, 180.
32. Choudhary, M. S.; Fink, J. K.; Lederer, K.; Krässig, H. A. Investigations of the action of flame retardants in cellulose. II: Investigation of the flame-retardant action of polyphosphonitride in cellulose. *J. Appl. Polym. Sci.* **1987**, *34*, 863–869.
33. Koch, E.-C.; Cudziło, S. Safer Pyrotechnic Obscurants Based on Phosphorus(V) Nitride. *Angew. Chem. Int. Ed.* **2016**, *55*, 15439–15442; *Angew. Chem.* **2016**, *128*, 15665–15668.
34. Passmore, E. M.; Duggan, G. L. Thermochemical Relationships for Phosphorous Getters in Gas-filled Incandescent Lamps. *J. Illum. Eng. Soc.* **1978**, *7*, 202–206.
35. Karau, F.; Schnick, W. A nitridic clathrate: $P_4N_4(NH)_4(NH_3)$. *Angew. Chem. Int. Ed.* **2006**, *45*, 4505–4508; *Angew. Chem.* **2006**, *118*, 4617–4620.
36. Marchuk, A.; Schnick, W. $Ba_3P_5N_{10}Br:Eu^{2+}$ : A Natural-White-Light Single Emitter with a Zeolite Structure Type. *Angew. Chem. Int. Ed.* **2015**, *54*, 2383–2387; *Angew. Chem.* **2015**, *127*, 2413–2417.
37. Schnick, W.; Luecke, J. Lithium ion conductivity of $LiPN_2$ and $Li_7PN_4$. *Solid State Ion.* **1990**, *38*, 271–273.
38. Bertschler, E.-M.; Dietrich, C.; Janek, J.; Schnick, W. $Li_{18}P_6N_{16}$ - A Lithium Nitridophosphate with Unprecedented Tricyclic $Li_{18}P_6N_{16}$ - Ions. *Chem. Eur. J.* **2017**, *23*, 2185–2191.
39. Bertschler, E.-M.; Bräuniger, T.; Dietrich, C.; Janek, J.; Schnick, W. $Li_{47}B_3P_{14}N_{42}$ - A Lithium Nitridoborophosphate with $[P_3N_9]^{12-}$, $[P_4N_{10}]^{10-}$, and the Unprecedented $[B_3P_3N_{13}]^{15-}$ Ion. *Angew. Chem. Int. Ed.* **2017**, *56*, 4806–4809; *Angew. Chem.* **2017**, *129*, 4844–4887.
40. Sedlmaier, S. J.; Eberspächer, M.; Schnick, W. High-Pressure Synthesis, Crystal Structure, and Characterization of $Zn_2PN_3$ - A New catena-Polynitridophosphate. *Z. Anorg. Allg. Chem.* **2011**, *637*, 362–367.
41. Landskron, K.; Irran, E.; Schnick, W. High-Temperature High-Pressure Synthesis of the Highly Condensed Nitridophosphates $NaP_4N_7$, $KP_4N_7$, $RbP_4N_7$, and $CsP_4N_7$ and Their Crystal-Structure Determinations by X-ray Powder Diffraction. *Chem. Eur. J.* **1999**, *5*, 2548–2553.
42. Kloss, S. D.; Schnick, W. Rare-earth-metal nitridophosphates through high-pressure metathesis. *Angew. Chem. Int. Ed.* **2015**, *54*, 11250–11253; *Angew. Chem.* **2015**, *127*, 11402–11405.
43. Vogel, S.; Buda, A. T.; Schnick, W. United in Nitride: The Highly Condensed Boron Phosphorus Nitride $BP_3N_6$. *Angew. Chem. Int. Ed.* **2018**, *57*, 13202–13205; *Angew. Chem.* **2018**, *130*, 13386–13389.
44. Eisenburger, L.; Weippert, V.; Paulmann, C.; Johrendt, D.; Oeckler, O.; Schnick, W. Discovery of Two Polymorphs of $TiP_4N_8$ Synthesized from Binary Nitrides. *Angew. Chem. Int. Ed.* **2022**, *61*, e202202014; *Angew. Chem.* **2022**, *134*, e202202014.

45. Marchuk, A.; Pucher, F. J.; Karau, F. W.; Schnick, W. A high-pressure polymorph of phosphorus nitride imide. *Angew. Chem. Int. Ed.* **2014**, *53*, 2469–2472; *Angew. Chem.* **2014**, *126*, 2501–2504.

46. Wendl, S.; Seidl, L.; Schüler, P.; Schnick, W. Post-Synthetic Modification: Systematic Study on a Simple Access to Nitridophosphates. *Angew. Chem. Int. Ed.* **2020**, *59*, 23579–23582; *Angew. Chem.* **2020**, *132*, 23785–23788.

47. Wendl, S.; Schnick, W. $SrH_4P_6N_{12}$ and $SrP_8N_{14}$ : Insights into the Condensation Mechanism of Nitridophosphates under High Pressure. *Chem. Eur. J.* **2018**, *24*, 15889–15896.

48. Hinuma, Y.; Hatakeyama, T.; Kumagai, Y.; Burton, L. A.; Sato, H.; Muraba, Y.; Iimura, S.; Hiramatsu, H.; Tanaka, I.; Hosono, H.; Oba, F. Discovery of earth-abundant nitride semiconductors by computational screening and high-pressure synthesis. *Nat. Commun.* **2016**, *7*, 11962.

49. Stock, A.; Grüneberg, H. Über den Phosphorstickstoff. *Ber. Dtsch. Chem. Ges.* **1907**, *40*, 2573–2578.

50. Aizawa, Y.; Yoneda, A. *P-V-T* equation of state of $MgSiO_3$ perovskite and MgO periclase: Implication for lower mantle composition. *Phys. Earth Planet. Inter.* **2006**, *155*, 87–95.

51. Oxford Instruments. *AZtecEnergy*, Abington, **2016**.

52. Juza, R.; Neuber, A.; Hahn, H. Zur Kenntnis des Zinknitrides Metallamide und Metallnitride. IV. Mitteilung. *Z. Anorg. Allg. Chem.* **1938**, *239*, 273–281.

53. Mann, J. B.; Meek, T. L.; Allen, L. C. Configuration Energies of the Main Group Elements. *J. Am. Chem. Soc.* **2000**, *122*, 2780–2783.

54. Fanfoni, M.; Tomellini, M. The Johnson-Mehl-Avrami-Kohnogorov model: A brief review. *Il Nuovo Cimento D* **1998**, *20*, 1171–1182.

SYNOPSIS

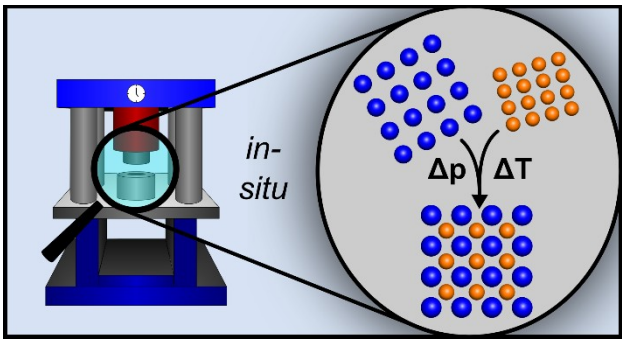


$Zn_2PN_3$ is used as a case study for the systematic *in-situ* investigation of a nitridophosphate HP/HT-synthesis. During compression and heating, the starting materials remain crystalline above their ambient-pressure decomposition points. At a minimum required temperature, the reaction starts via ion diffusion at grain boundaries with an exponential decay of the reaction rate. Higher temperatures complete the reaction quickly and initiate singly crystal growth. Cooling and decompression steps show no significant impact on the resulting product.